Nanoscale

PAPER

View Article Online
View Journal | View Issue

Cite this: *Nanoscale*, 2023, **15**, 14205

Highly stretchable hydroxyapatite bionanocomposite for high-performance triboelectric nanogenerators†

Thien Trung Luu,[a] Nghia Dinh Huynh,[a] Hakjeong Kim,[a] Zong-Hong Lin*[b] and Dukhyun Choi *[a,c]

Renewable energy has been a focus in recent years. Triboelectric nanogenerators (TENGs) have potential for converting mechanical energy into electricity. However, there are restrictions on the use of biological materials and bionanocomposites, such as the high cost and complexity of the synthesis process, poor stability, and inadequate output performance. To overcome the constraints of TENGs, we have turned to hydroxyapatite, a biological substance with great biocompatibility and high mechanical strength that can be manufactured from waste materials. We successfully developed a negative triboelectric bionanocomposite hydroxyapatite (HA) loaded polydimethylsiloxane (PDMS) to harness energy from biomechanical sources such as wearable devices. A TENG (2×2 cm^2) with a pushing force of 2 N and different amounts of HA in PDMS can produce highly stable output voltage, current, surface charge density, and power density values of 300 V, 22.4 μA, 90.36 μC m^{-2}, and 27.34 W m^{-2}, which are 6, 9, and 10 times higher than those without HA, respectively. These improvements were attributed to the highest observed surface potential of 1512 mV. After 20 000 cycles of contact-separation, the HA/PDMS-TENG shows exceptionally stable performance. Furthermore, adding HA improves the mechanical properties and the stretchability of the bionanocomposite. The HA/PDMS bionanocomposite exhibits remarkable stretchability of more than 290%. Effectively harvesting energy from body movements, the TENG gadget may be used to charge multiple commercial capacitors, drive up to 100 LEDs, and power a low-power electronic device. Self-powered sensing and wearable devices are made possible by the HA/PDMS-TENG, which allows their large-scale preparation and deployment.

Received 15th June 2023,
Accepted 10th August 2023

DOI: 10.1039/d3nr02849f

rsc.li/nanoscale

1. Introduction

In light of the growing awareness of the harmful impacts of climate change and pollution, adopting renewable energy sources like wind, water, and sunshine has taken on greater significance in recent years. Greenhouse gases and other pollutants are emitted at far lower rates from renewable energy sources than from conventional fossil fuels,[1] making them a valuable tool in the fight against global warming. Our reliance on limited nonrenewable resources, which have adverse environmental effects when harvested and exploited, is also reduced when using renewable energy sources.[2] In 2012, Wang's team developed the first TENG,[3] which can function in one of four main operating modes: vertical contact separation, in-plane contact sliding, a single electrode, or a freestanding triboelectric layer.[4] TENGs are an innovative technology that make use of electrification and electrostatic induction to convert unpredictable mechanical energy created by human actions (such as hand tapping or walking) and natural events (such as wind, waves, or rain) or vibrations from vehicles into an electrical current.[5–15]

Various technologies have been used to achieve high performance such as plasma processing,[16,17] 3D-surface pattern lasers,[18,19] layer by layer assembly,[20–22] electron blocking layers,[23,24] porous materials,[25,26] thermal imprinting lithography,[27] charge-trapping effects,[18] ultrasound technique,[28,29] high dielectric constant materials (*e.g.*, barium titanate loaded polydimethylsiloxane (PDMS), strontium-doped barium titanate loaded PDMS),[13,30–35] and the electron double layer effect.[36] These technologies have increased output performance. However, TENGs are difficult to produce on a large scale

---

[a] *School of Mechanical Engineering, College of Engineering, Sungkyunkwan University, 2066, Seobu-ro, Jangan-gu, Suwon, Gyeonggi 16419, South Korea. E-mail: bred96@skku.edu*

[b] *Department of Biomedical Engineering, National Taiwan University, Taipei, 10617, Taiwan*

[c] *Institute of Energy Science & Technology (SIEST), Sungkyunkwan Univeristy, 2066, Seobu-ro, Jangan-gu, Suwon, Gyeonggi 16419, South Korea*

† Electronic supplementary information (ESI) available. See DOI: **https://doi.org/10.1039/d3nr02849f**

due to the complicated process and the expensive materials and equipment.

Several natural materials have been discovered with the ability to harvest electric energy from mechanical power sources, ensuring low-cost production while also being ecologically safe and biocompatible during continuous or intermittent contact with the human body. Biocompatible materials are essential for many uses, including those involving direct skin contact or implantation into the body (such as in cutting-edge biomedical sensors that monitor everyday activity and multifunctional medical devices). However, the exploitation of high-performance output from natural materials is still relatively limited. Still need more improvement when compared to other materials.[37,38]

$Ca_5(PO_4)_3OH$, also known as hydroxyapatite (HA), is a crucial biomaterial used in bone implants and dentistry.[39] The unique features of HA make it both a biocompatible and a bioactive substance. HA forms direct links with bone and promotes implant attachment. To the best of our knowledge, no HA-based bionanocomposite-TENG has been reported. In addition, one of the highlights of HA is that it can be synthesized from abundant natural resources. HA is typically obtained from animal bones (such as those of cows, camels, and horses),[40,41] eggshells,[42] and algae materials,[43] as well as inorganic materials like limestone.[44] The dielectric constant of HA is high (even greater than the dielectric constant of pristine PDMS) at low frequencies. As a result, HA is a promising filler choice with the potential to enhance both material attributes and output performance.[45,46]

Herein, we provided low-cost, high-stretchable, and translucent HA/PDMS bionanocomposites for high-performance, wearable, and biomechanical TENGs. We analyzed dielectric constant, mechanical characteristics, surface potential, and surface roughness for HA/PDMS films according to the amount of HA. The electrical behaviors of HA/PDMS based TENG (HA-TENG) were investigated. The HA-TENG with 10% HA showed highly stable electrical output with a voltage of 300 V, a current of 22.4 μA, and respective charge and power densities of 90.36 μC m^{-2} and 27.34 W m^{-2}. The HA-TENG could be used to drive 100 LEDs, to charge multiple commercial capacitors, and to drive electronic devices. Furthermore, HA-TENG were connected to various human body parts (*e.g.*, lap, arm), a cloth, and an insole to collect energy and track human movement, such as walking, running, and hand tapping. Our study will give a chance for using waste biomaterials for high-performance ecofriendly TENGs.

2. Experimental section

2.1. Material

Silicon elastomer (PDMS Sylgard-184) was purchased from 4science (Korea) and HA powder [$(Ca_5(PO_4)_3OH)$, average particle size <5 μm, surface area ≥80 m^2 g^{-1}] was purchased from Sigma-Aldrich. All the materials were used as received without any further purification.

2.2. Fabrication process of HA/PDMS composite

Various HA-loaded PDMS-based bionanocomposite films were fabricated by mixing HA into the PDMS solution. The fabrication process of HA/PDMS bionanocomposite began by mixing a PDMS elastomer and cross linker (Sylgard 184, Dow Corning) in a 10 : 1 weight ratio. Hydroxyapatite powders (average particle size <2.5 μm, surface area ≥80 m^2 g^{-1}) in different weight percentages (0, 1, 2, 5, 8, 10, 14, 18, 24 wt%) were added to the PDMS mixture until all particles were homogeneously dispersed in the solution. The samples were named *x*HA/PDMS, where *x* is the HA weight percentage. The resulting mixture was blended using a planetary centrifugal mixer (ARE-310, Thinky Co.) at a revolution speed of 2000 rpm for 3 minutes. The blended HA/PDMS mixture was subsequently cast onto 2 × 2 cm^2 aluminum plates using spin coating at 300 rpm for 30 s and then 450 rpm for 45 s. The bionanocomposite film was thermally cured at 80 °C for 2 hours. No solvent or sacrificial templates were required in the process.

2.3. Fabrication and output measurement of the HA-TENG

To design the vertical contact-separation mode TENG device, the top electrode was prepared with a 2 × 2 cm^2, 80 μm-thick commercial aluminum foil that was cleaned with ethanol and dried in flowing N_2 gas. The aluminum foil was attached to a polylactic acid (PLA) substrate using double-sided foam tape. Subsequently, a flat PDMS film or HA/PDMS was carefully laminated onto the PLA substrate to prepare the TENG bottom electrode. Herein, the HA/PDMS and Al were employed as the triboelectric layer and the bottom electrode of the TENG, respectively. Another 2 × 2 cm^2 Al foil was attached to the PLA substrate in which double-sided foam tape was utilized as the top part or plate of the TENG. The Al foil on the top plate of TENG can also serve as an electrode. Finally, the top and bottom parts of the TENG device were combined with a separation gap of 5 mm and were connected by an electric wire attached to both electrodes.

2.4. Characterization and simulation

The output of the TENG was measured by applying a force with a pushing tester (model number JIPT-120, manufactured by Junil Tech). After joining the two electrodes of the TENG device together with a gap of 5 mm. The output of a TENG was measured when a force of 2 N was exerted on the device while it was operating at a frequency of 5 Hz and 35% humidity of environment. To determine the voltage at the TENG output, a Tektronix MDO3052 mixed domain oscilloscope with a 40 MΩ input impedance was used. Current was measured from a Stanford Research Systems SR570 low-noise current preamplifier with the assistance of a Tektronix MDO3052 mixed domain oscilloscope. The amount of charge moved was determined using a Keithley 6514 electrometer. Analysis of the surface morphology and cross-sectional structure of both the flat PDMS film and the HA/PDMS film was performed by field emission scanning electron microscopy (FE-SEM; S-4800, Hitachi, Japan). An atomic force microscope (AFM, model

NX10 available from Park Systems Corp.) was used to assess the surface potential and surface morphology. Using an FT-IR spectrophotometer (NICOLETiS5, Thermo Scientific) with 32 linear scans and 8 cm^{-1} resolution, we collected attenuated total reflection Fourier-transform infrared (ATR-FTIR) spectra. The specific capacitance of the fabricated bionanocomposite films was measured with an LCR meter (Hewlett Packard 4282A). The mechanical properties of HA/PDMS films were determined using a universal testing machine (AGX-20kNVD with a 50 N load cell, SHIMADZU, Japan) and Nanoindentation – NanoTest Vantage (Micro Materials).

We used finite element modeling (using the program COMSOL Multiphysics) to assess the charge distribution across the TENG electrodes to supplement the experimental investigation of the HA-TENG. The HA-TENG model was contrasted with the PDMS-TENG model in the theoretical model. In the simulations, the dielectric constant, area size, and thickness of the optimal HA layer were included for the HA-TENG simulations. Additionally, we assumed a 90.36 μC m^{-2} tribocharge density between the TENG electrodes.

3. Results and discussion

The procedure for synthesizing HA/PDMS is shown in a schematic in Fig. 1a. FE-SEM images were used to analyze the consistent deposition of HA as well as the morphologies of the microstructured HA/PDMS bionanocomposite surface. The HA particles are evenly distributed throughout the PDMS, with particles ranging in size from 0.4 μm to 1.6 μm dispersed widely throughout the PDMS, and 2.4 μm to 3.6 μm particles found in very low numbers (Fig. 1b. The elemental characterization and EDS images are shown in Fig. 1c and Fig. S1.† HA is the source of Ca and P, and the results suggest that it is widely dispersed over the bionanocomposite's microstructured surface. These bionanocomposites had a thickness of 178 μm (Fig. 1d) through the cross-section image of FE-SEM. In addition, as in Fig. 1e, there are translucent films present in the bionanocomposite material; the UV-VIS transmittance spectra also confirmed this argument (Fig. S3†). Fourier transform infrared HA/PDMS attenuated total reflectance (ATR-FTIR) spectroscopy was used to assess the ionic interactions between HA and PDMS (Fig. S2†). Between 3568 cm^{-1} and 636 cm^{-1} (wide OH^- ion stretching and bending, respectively), the PDMS spectra showed the classic peaks for HA.[47,48] The (PO_4^{3-}) ion was identified by its peaks at 600 cm^{-1} and 563 cm^{-1}. These findings demonstrate that HA is an integral part of the PDMS structure. Digital pictures of all *x*HA/PDMS films demonstrate that the addition of HA particles transformed the previously transparent PDMS into a uniformly opaque white (Fig. 1e). Furthermore, Fig. 1f exhibits a high stretchability of HA/PDMS, which will be further tested and

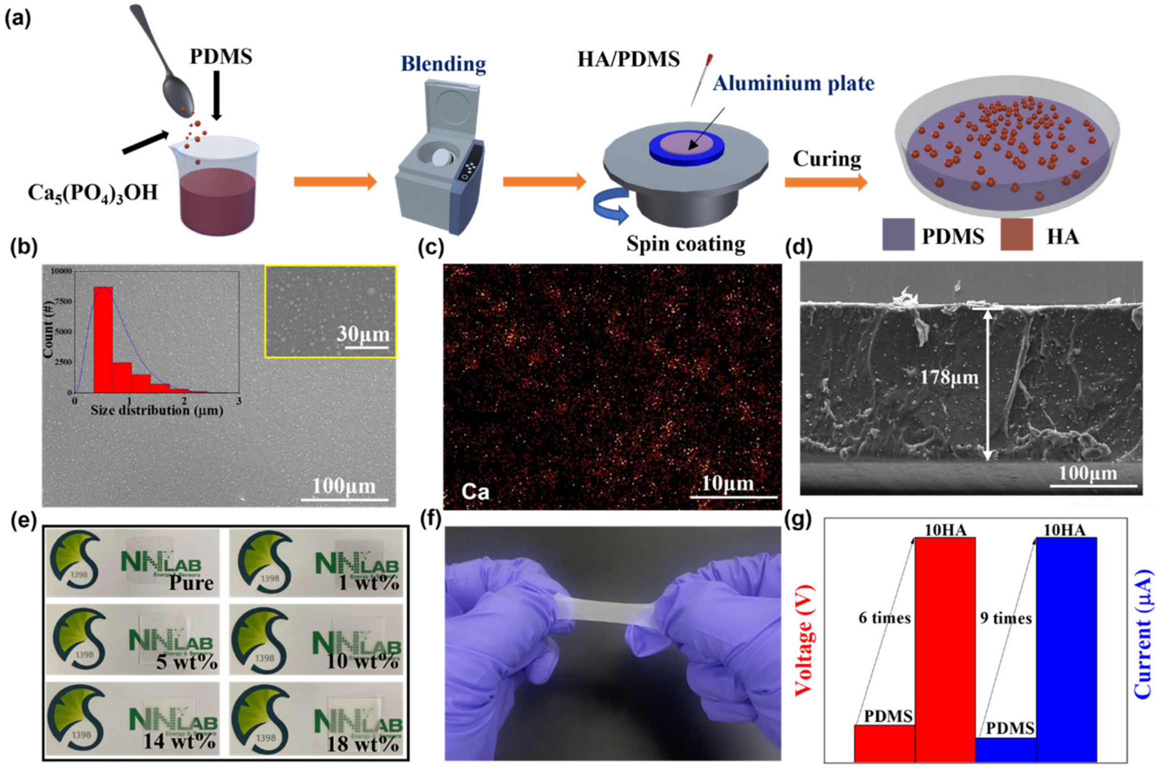

Fig. 1 (a) Schematic illustration of the fabrication process of HA/PDMS bionanocomposite. (b) 3D structure of HA/PDMS bionanocomposite. (c) FE-SEM images of the HA/PDMS. (d) Energy dispersive spectrometry (EDS) images of the HA/PDMS bionanocomposite. (e) Cross-sectional FE-SEM image of the bionanocomposite. (f) Photographs demonstrating the stretchability of HA/PDMS. (g) Enhancing output performance of triboelectric nanogenerator *via* HA/PDMS compared to pristine PDMS.

discussed in the mechanical properties testing. In addition, the HA-TENG indicated excellent output performance, which improved 6 times and 9 times for voltage and current, respectively (Fig. 1g).

Analysis of ultra nanoindentation and tensile tests showed that the HA/PDMS film was mechanically suitable for use as a nanogenerator (Fig. 2a–d). Ultra-nanoindentation (Fig. 2a) was performed five times on the HA/PDMS film (180 μm thickness) at a maximum loading of 1 mN using the Oliver and Pharr technique. The load-displacement curves show that, by including additional HA in the PDMS, the average elastic modulus and hardness were increased and reached their maximum displacement values of 6953 nm at a 10 s pause (Fig. 2a and b). Previous research has shown that HA can improve the mechanical characteristics of composites.[49–51] The mechanical tensile test of the HA/PDMS film was conducted five times at 25 °C (Fig. 2c). Compared to a pure PDMS sample, the film stretchability was dramatically enhanced by adding HA. The percentage of elongation became closer to 300% for 24HA/PDMS samples as the concentration of HA increased. To prove the real photograph of stretchability, we show the initial state when conducting the tensile test (Fig. 2d(i)) and after stretching (Fig. 2d(ii)). Furthermore, we demonstrated that the initial rectangular piece of 10HA/PDMS with a length of 2.2 cm could be easily stretched to more than 5.5 cm, as in Fig. S4,† which translates to a stretchability of at least 250%. Increased mechanical parameters like ultimate tensile strength and compressive yield strengths are probably due to the even distribution of stiff HA particles in the PDMS (Fig. 1b). As is common with organic/inorganic composites, the HA phase may be much stiffer than the flexible PDMS,[52,53] and an interlocking effect[21,51] allowed the composite to better retain applied stresses. As could be expected, tensile strength decreased when loaded with 24HA/PDMS. This might be because HA forms large spaces on the surface due to its poor aggregation and dispersion (Fig. S1†). Furthermore, according to the phenomena described above, the degree of hydrogen bonding increases as HA percentage increased. *In situ* repair after damage and chain reorientation in the stretching direction are possible due to the reversible assembly–disassembly of hydrogen bonds.[54,55]

The roughness of the surfaces of the triboelectric layers, the surface potential, and the dielectric properties were some of the many factors that were investigated to explain the high

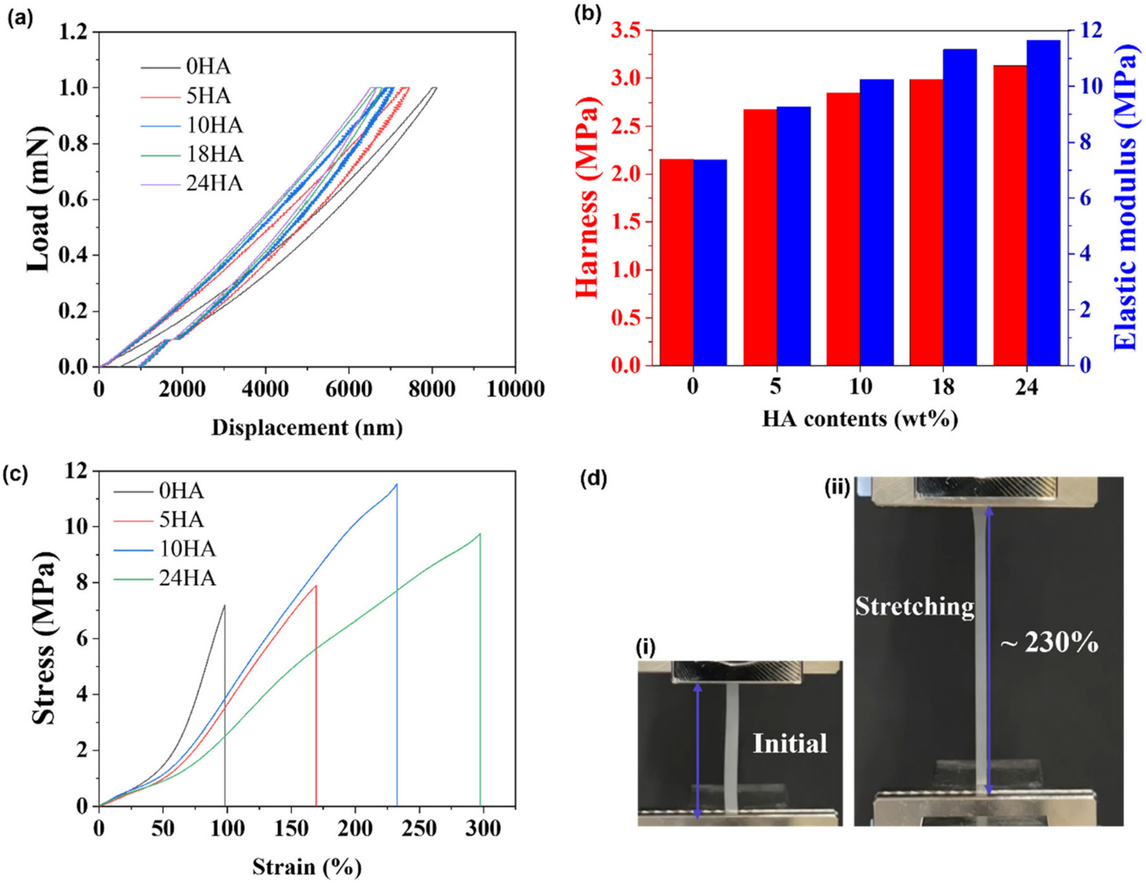

Fig. 2 (a) Load-displacement (depth) curve of HA/PDMS thin film *via* nanoindentation. (b) Harness and elastic modulus of HA/PDMS with different contents of hydroxyapatite. (c) Tensile stress–strain curve of HA/PDMS bionanocomposite with different hydroxyapatite contents. (d) Digital image of 10HA/PDMS before and after stretching.

output using HA/PDMS. The charge transfer density can be increased by increasing the surface potential, and the charge transfer processes may be enhanced by tailoring the surface charge characteristics. Furthermore, with the higher the roughness, there will be important factors to increase the output performance of TENG. In the initial step of this process, which is shown in Fig. 3c, we evaluated the surface roughness of these triboelectric materials using AFM. The values for the root mean square roughness of *x*HA/PDMS at 0–5–10–14–18 were 1.73, 10.32, 16.6074, 15.93, and 15.623 nm, respectively. The discernible increase in surface roughness lends credence to the theory that this property plays a significant role in increasing outputs.[20,21,56] The AFM results demonstrate that increasing the amount of HA in PDMS causes an increase in surface roughness, which in turn helps to improve triboelectrification. Although there was a small decrease in the root mean square, this behavior cannot explain the decrease in production despite the increase in content density. According to these findings, the HA/PDMS bionanocomposite film's surface is rougher than that of the PDMS film. We performed surface potential measurements to confirm the triboelectric negative surface capacity of the HA/PDMS bionanocomposites. Fig. 3d presents the results of Kelvin probe force microscopy (KPFM), which revealed the surface potential of these bionanocomposites. This is also one of the parameters required to demonstrate increased output performance.[20,23,57] When 10HA/PDMS was added, the surface potential jumped from 400 mV to 1512 mV. The relative change in surface potential further confirmed the inferences that high HA content will impair the triboelectric polarity of bionanocomposite and that the triboelectric polarity of triboelectric materials can be effectively improved by a triboelectric coating to boost triboelectric charge generating capability. Furthermore, the decrease in surface potential when the content increased from 14–18HA/PDMS partly explained why the output performance was significantly reduced compared to that of 10HA/PDMS.

Under a 2 N excitation force and 5 Hz frequency under ambient settings, the TENG device voltage and current were measured to analyze its electrical performance. TENGs based on HA/PDMS bionanocomposite films with the same thickness were measured for electrical output, short-circuit current, open-circuit voltage, and transfer charge under the same conditions (Fig. 4a–c). This allowed comparison of TENG performance across a range of HA concentrations. HA-TENG had much larger open-circuit voltage and short-circuit current in comparison to pure PDMS-TENG. The output current and voltage of the TENG increased gradually when the amount of HA was increased to 10HA/PDMS, reaching 22.4 μA and 300 V, respectively. These are 9 times and 6 times those of pure PDMS, which has outputs of 2.5 μA and 50 V, as illustrated in Fig. 4a

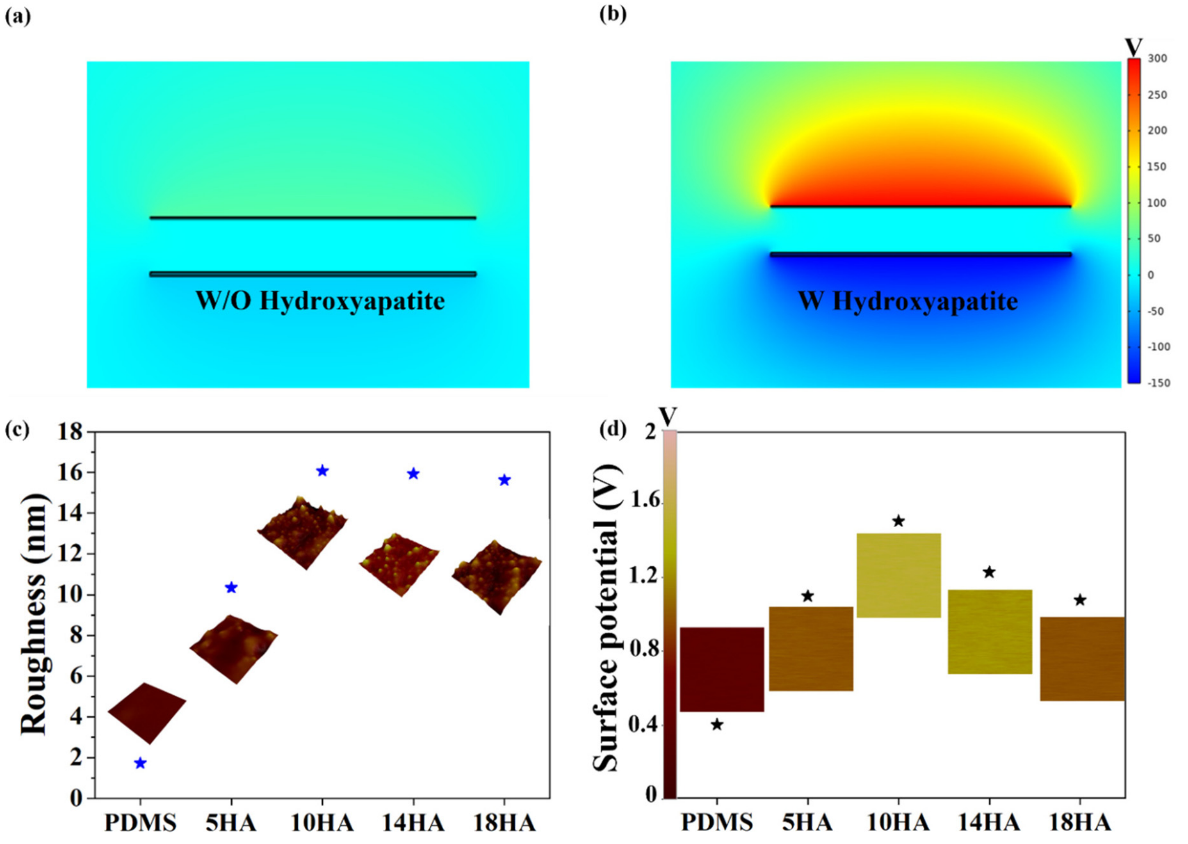

Fig. 3 (a and b) Comsol simulations with and without hydroxyapatite. (c) Surface morphology and (d) surface potential of HA/PDMS bionanocomposite films were obtained by AFM.

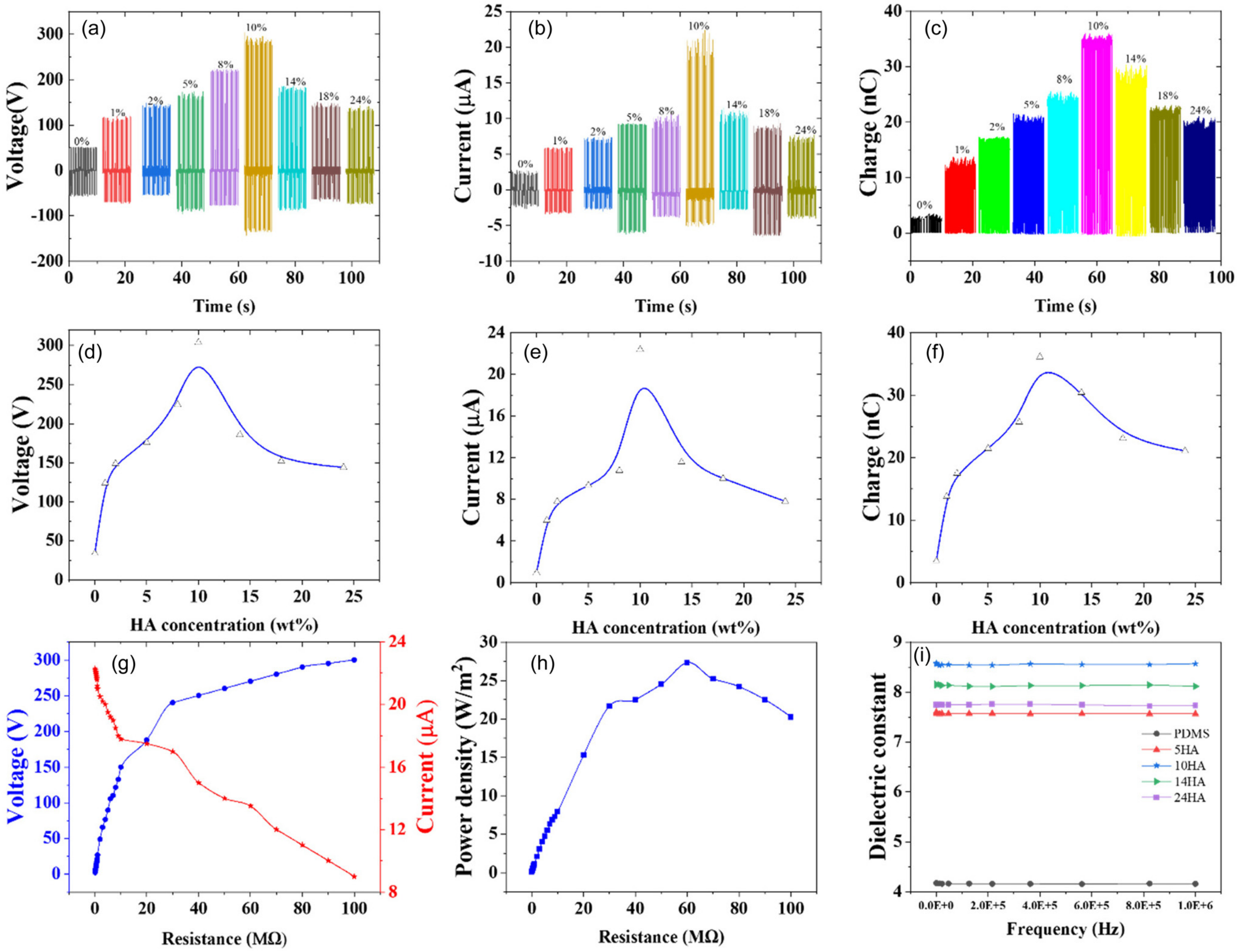

Fig. 4 Effect of weight ratio of hydroxyapatite on the electrical output. (a) Voltage, (b) current and (c) transfer charge signals of HA-TENG as a function of time. Variation of (d) voltage, (e) current, and (f) transfer charge signals produced from TENG device with various ratios of HA. (g) The current, voltage, and (h) power density of TENG based on bionanocomposite film with 10HA/PDMS as a function of external load resistance ranging from 0.1 MΩ to 100 MΩ. (i) Dielectric constants of various HA/PDMS bionanocomposite films.

and b. When increasing the amount of HA from 14HA/PDMS to 24HA/PDMS, the output current and voltage both decreased. The output current and voltage initially increase with an increase in filling weight ratio and then decrease. Powder tends to agglomerate as concentration increases, resulting in segregated clusters rather than a uniform mixture, which explains this behavior.[30] Once the HA concentration in the bionanocomposite film increased above 14 wt%, the particles began to agglomerate within the composite film, as seen in Fig. S1.† The HA/PDMS showed a decreasing trend in electrical output. The transfer charge and short-circuit current tend to decrease. Fig. 4d–f also illustrates the link between the ratios of HA present in the bionanocomposite films and the short-circuit current, open-circuit voltage, and transfer charge of the TENGs. TENG open-circuit voltage, short-circuit current, and transfer charge were all at their maximum observed levels when the HA concentration was 10% by weight. Fig. 4g illustrates the relationships between the external load resistance (in the range of 0.01 MΩ to 100 MΩ) and the output current and voltage of a TENG based on a bionanocomposite film that contains 10HA/PDMS. The resistance of the external load ranged from 0.01 MΩ to 100 MΩ. When the connected external resistance increased, the output voltage also increased, but the output current decreased. It is possible to calculate the instantaneous power output of the TENG if resistors are used to monitor the load voltage and current (Fig. 4h). The TENG had a maximum output power density of about 27.34 W m^{-2} when it was loaded with a resistance of 60 MΩ. An increase in dielectric constant would have a major impact on the efficiency of the TENG electric output. As in Fig. 4i, we measured the dielectric constant of HA/PDMS films at frequencies ranging from 10 kHz to 1 MHz. At a frequency of 100 Hz, the 10HA/PDMS had a dielectric constant of 8.6, which was significantly higher than that of the pure PDMS sample. This finding corroborates prior research showing that HA has a high dielectric constant at low frequencies, and it also satisfies the criteria for inclusion in the category of materials with a large dielectric constant.[58,59] In addition, the decreases in dielectric constant, surface potential, and agglomeration observed when increasing the HA content above 10% also contributed to the decrease in TENG output performance when adding more HA to the PDMS.

Fig. S5† shows a schematic of the HA/PDMS device function. Furthermore, Fig. 3a and b depicts a comparison between pristine PDMS and HA/PDMS friction layers based on theoretical simulations. In the initial condition (i) without any external force imposed on the TENG, there is no electrostatic distribution at the electrodes, as shown in Fig. S5a.† Contact electrification occurred between the HA/PDMS and top Al electrodes when an external force was applied to the TENG *via* the top plate (ii). This caused the two electrodes to possess opposing electrostatic charges. When the external force was removed, the two contacting surfaces of the layers separated (iii), creating a potential difference between the HA/PDMS and the top Al. To achieve electrical balance, electrons flowed from the bottom Al electrode to the top Al electrode through the external circuit, driven by the potential difference between the electrodes. When the electrodes are in their fully separated (iv) state, the triboelectric charges scattered on the bottom Al–HA/PDMS return to their original levels. Because of this, the two electrodes are brought closer together when an external force is applied to the TENG, inducing an electrostatic potential difference in the opposite direction. This causes electrons to flow from the top electrode to the bottom electrode. Therefore, the TENG operates repeatedly because of the applied cyclic pushing force. Fig. 3a and b from the COMSOL Multiphysics simulation show the surface charge distribution and electric potential shift between two TENG electrodes when an external pushing force is applied to separate the top plate of the TENG. Here, we see how the PDMS-TENG is in comparison with HA-TENG in a theoretical simulation. The measured electrical output and the charge created (as shown in Fig. S5b†) were matched in the simulation.

Using the charging curves shown in Fig. 5a, the PDMS and 10HA/PDMS were compared in charge behavior. Compared to

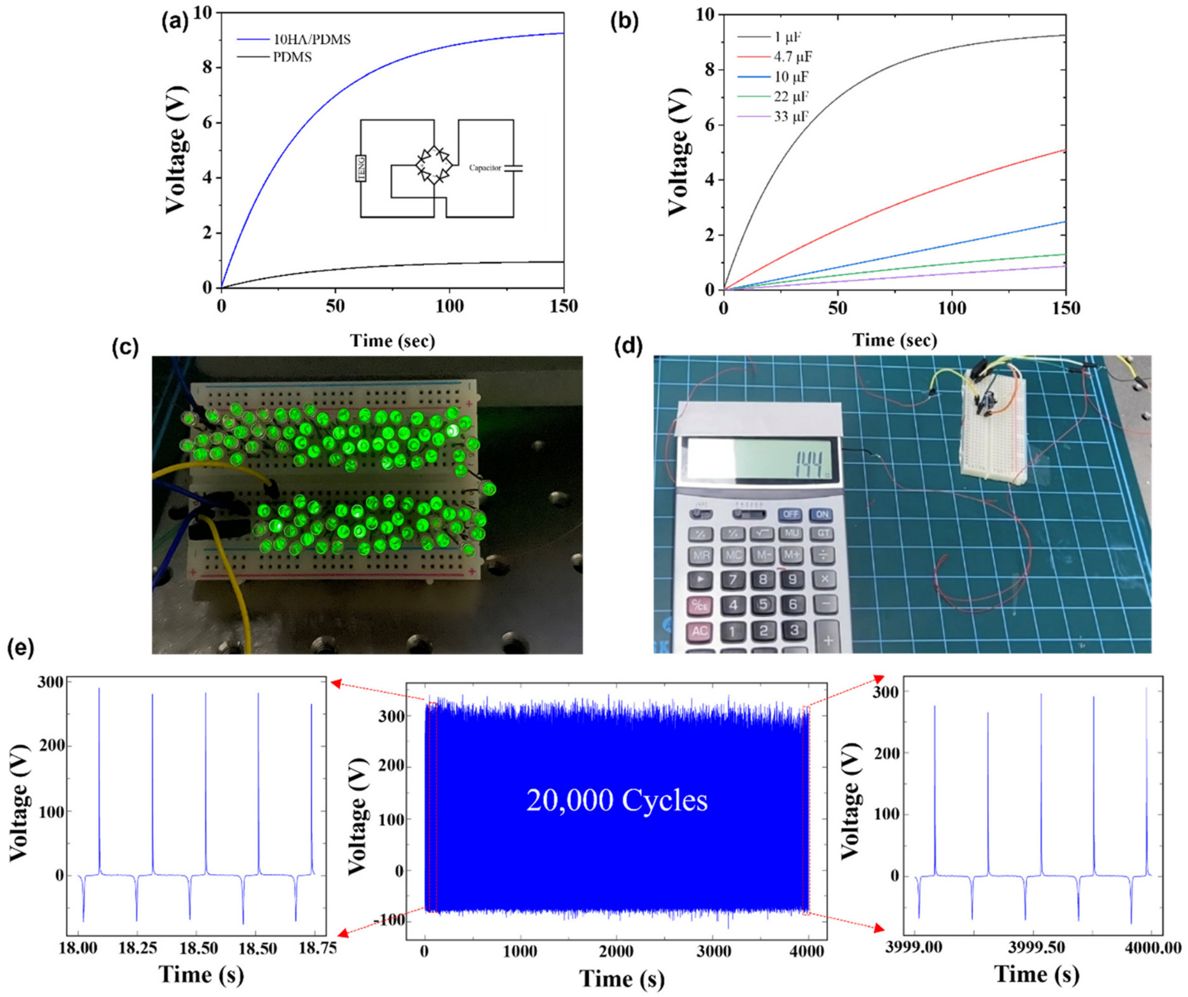

Fig. 5 (a) The charging curves of a 1 μF capacitor comparing PDMS and optimal 10HA/PDMS at an input frequency of 5 Hz and an applied force of 2 N. (b) The charging curves of different capacitors with optimized 10HA/PDMS at an applied force of 2 N. (c and d) HA-TENG powering 100 LEDs or a commercial calculator. (e) Endurance test of the optimized HA-TENG for more than 20 000 cycles.

PDMS, the 10HA-TENG was about 8.5 times quicker in charging a capacitor with a capacity of 1 μF when the input frequency was 5 Hz and the applied force was 2 N. The HA-TENG was also used to charge a variety of capacitors with capacities ranging from 1 to 4.7–10–22–33 μF for a total of 150 seconds, as Fig. 5b demonstrates. Capacitors with 33–1 μF capacitances have a linear increase in output charging rate, allowing their use in real-world applications (such as powering LED lights or operating commercial calculators). Fig. 5c illustrates how the 10HA/PDMS was used to demonstrate the serial connection by switching on 100 LED lights using a pushing tester that exerted a force of 2 N (as shown in ESI Movie S1†). When the HA-TENG was tested with 5 Hz of contact separation delivered with 2 N of force from a pushing machine, more than 2 V was stored in the capacitor. After being connected to a 10 μF capacitor charged to greater than 2 V *via* the HA-TENG, the fundamental arithmetic operations were completed in 8 s (as shown in ESI Movie S2, and Fig. S6 in ESI†). Furthermore, compared to the maximum performance of the HA-TENG, the maximum performance of a variety of TENGs based on high dielectric constant materials was examined. In this experiment, the HA-TENG showed outstanding output performance, while other materials, as stated in Table S1,† require rather complex fabrication or are expensive.

An endurance test was also carried out to further confirm the HA-TENG superior mechanical stability and durability in comparison to the optimum 10HA/PDMS. As a result, 20 000 contact-separation cycles were used such that the V values of the HA-TENG could be calculated (Fig. 5e). According to the findings, the amplitudes of the TENG output voltage experienced very little to no change after 20 000 pressing cycles. Therefore, our HA-TENG delivered a constant output during a large range of pushing cycles, indicating that it is feasible to create a TENG with a significantly prolonged useful life for actual industrial use. This was demonstrated by the survival of our TENG through the whole range of pushing cycles.

In addition to this, we evaluated the performance of the 10HA/PDMS film using an HA-TENG based on skin electrodes. The results, which are shown in Fig. 6a, indicate the good function of the 10HA-TENG (for example, 290, 280, and 120 on

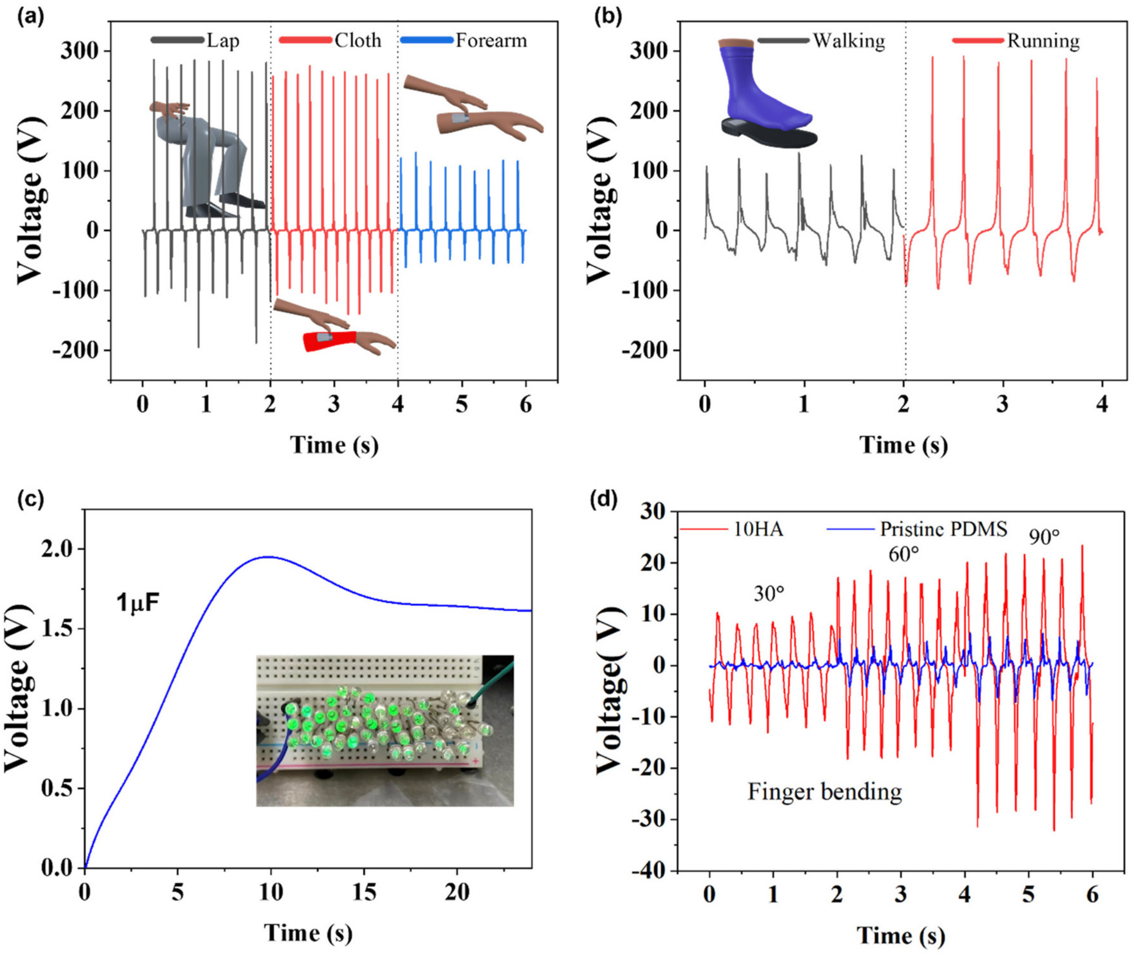

Fig. 6 HA-TENG as a skin-patchable encodable touch sensor and wearable sensor for human activities. (a) Various HA-TENG applications attached on various substrates (*e.g.*, lap, cloth, forearm) and their triboelectric output voltages. (b) Schematic of HA-TENG-implanted insole and its triboelectric output voltages. (c) LED lighting and capacitor charging are possible after 10 min of running. (d) Comparison of voltage response caused by finger bending between pristine PDMS and 10HA/PDMS.

the lap, fabric, and forearm, respectively, as shown in ESI Movies S3–S5†). Because of this, HA-TENG with a single electrode was constructed, as in Fig. 6b (HA-TENG contained inside the shoe). In addition, it acts as a model for automatic identification of human movement. When equipped on a person, the HA/PDMS insole can record a variety of signals. The output voltage increased from 100 V to 300 V as the subject progressed from walking to running. To demonstrate the HA-TENG's mechanical integrity, running motion was analyzed for 10 min (Fig. 6c). The energy created in this length of time charged a single capacitor with a capacity of 1 μF and powered 50 LEDs (as shown in ESI Movies S6 and S7†). To investigate human mechanical motion, we included laboratory rubber gloves as a positive friction material and the bionanocomposite negative friction structure of the HA-TENG to demonstrate use of the HA-TENG as a self-powering sensor with separate output signals. Fig. 6d illustrates how the self-powered device reacted electrically (and in real time) to changes in the bending and straightening indices of the finger joints such that it could detect physiological motion better than pristine PDMS (as shown in ESI Movie S8†).

4. Conclusion

In summary, we constructed a simple, translucent, high stretchability, and high-performance HA/PDMS bionanocomposite film-based TENG to synergistically capture external mechanical energy into electricity. The influence of different amounts of HA inside PDMS triboelectric film on the electrical output produced was systematically analyzed. The 10HA-TENG exhibited higher surface charge density of 90.36 μC m^{-2} and surface potential of 1512 mV than pristine PDMS. As a result, the 10HA-TENG produced the maximum electrical output, which generated the optimal performance in terms of voltage, current, charge density, and power density (300 V, 22.4 μA, 90.36 μC m^{-2} and 27.34 W m^{-2}, respectively) under a contact load of 2 N. These values are 6 times, 9 times, and 10 times higher than that of pristine PDMS-TENGs, respectively. It also showed exceptional durability and reliability for more than 20 thousand cycles of contact-separation. The HA-TENG were also used to charge different dielectric capacitors, drive 100 LEDs, and power a commercial calculator. Moreover, we attached HA-TENG to cloth, skin, an insole, and a person's lap. The proposed stretchable and designable negative triboelectric material developed through an inexpensive process could be used to fabricate high-performance biomechanical TENG devices and facilitate the advancement of portable electronic device technology.

Author contributions

Thien Trung Luu: conceptualization, methodology, experiments, writing – original draft. Nghia Dinh Huynh: conceptualization, methodology, experiments. Hakjeong Kim: formal analysis, experiments. Zong-Hong Lin: methodology, supervision. Dukhyun Choi: writing – review & editing, methodology, supervision.

Conflicts of interest

The authors declare no conflict of interest.

Acknowledgements

This work was supported by the Technology Innovation Program (20013794, Center for Composite Materials and Concurrent Design) funded by the Ministry of Trade, Industry & Energy (MOTIE, Korea). This research was also supported by National R&D Program through the National Research Foundation of Korea(NRF) funded by Ministry of Science and ICT(2022M3D1A2054488).

References

1 A. Kalair, N. Abas, M. S. Saleem, A. R. Kalair and N. Khan, *Energy Storage*, 2021, **3**, e135.

2 A. G. Olabi and M. A. Abdelkareem, *Renewable Sustainable Energy Rev.*, 2022, **158**, 112111.

3 F. R. Fan, Z. Q. Tian and Z. L. Wang, *Nano Energy*, 2012, **1**, 328–334.

4 S. M. Niu and Z. L. Wang, *Nano Energy*, 2015, **14**, 161–192.

5 V. Bui, N. D. Huynh, N. M. Chau, W. Kim, H. Kim, I. Oh, D. P. Huynh and D. Choi, *Nano Energy*, 2022, **101**, 107612.

6 K. D. Pham, D. Bhatia, N. D. Huynh, H. Kim, J. M. Baik, Z. H. Lin and D. Choi, *Nano Energy*, 2021, **89**, 106305.

7 W. Kim, K. D. Pham and D. Choi, *Nano Energy*, 2023, **106**, 108088.

8 W. H. Xu, H. X. Zheng, Y. Liu, X. F. Zhou, C. Zhang, Y. X. Song, X. Deng, M. Leung, Z. B. Yang, R. X. Xu, Z. L. Wang, X. C. Zeng and Z. K. Wang, *Nature*, 2020, **578**, 392–396.

9 C. S. Wu, A. C. Wang, W. B. Ding, H. Y. Guo and Z. L. Wang, *Adv. Energy Mater.*, 2019, **9**, 1802906.

10 G. Zhu, B. Peng, J. Chen, Q. S. Jing and Z. L. Wang, *Nano Energy*, 2015, **14**, 126–138.

11 W. Kim, D. Bhatia, H. J. Hwang, K. Choi and D. Choi, *Funct. Compos. Struct.*, 2019, **1**, 035003.

12 W. W. Du, Z. K. Li, Y. L. Zhao, X. Zhang, L. L. Pang, W. Wang, T. Jiang, A. F. Yu and J. Y. Zhai, *Chem. Eng. J.*, 2022, **446**, 137268.

13 J. Kim, H. Ryu, J. H. Lee, U. Khan, S. S. Kwak, H. J. Yoon and S. W. Kim, *Adv. Energy Mater.*, 2020, **10**, 2070040.

14 X. Zhang, Z. K. Li, W. N. Du, Y. L. Zhao, W. Wang, L. N. Pang, L. Chen, A. F. Yu and J. Y. Zhai, *Nano Energy*, 2022, **96**, 107115.

15 M. He, W. N. Du, Y. M. Feng, S. J. Li, W. Wang, X. Zhang, A. F. Yu, L. Y. Wan and J. Y. Zhai, *Nano Energy*, 2021, **86**, 106058.

16 X. Sun, Y. J. Liu, N. Luo, Y. Liu, Y. E. Feng, S. G. Chen and D. A. Wang, *Nano Energy*, 2022, **102**, 107691.

17 Y. Ra, J. H. Choi, M. La, S. J. Park and D. Choi, *Funct. Compos. Struct.*, 2019, **1**, 045001.

18 Y. W. Kim, H. B. Lee, J. Yoon and S. H. Park, *Nano Energy*, 2022, **95**, 107051.

19 M. Muthu, R. Pandey, X. Z. Wang, A. Chandrasekhar, I. A. Palani and V. Singh, *Nano Energy*, 2020, **78**, 105205.

20 H. G. Menge, N. D. Huynh, C. Cho, D. Choi and Y. T. Park, *Composites, Part B*, 2022, **230**, 109513.

21 H. G. Menge, N. D. Huynh, H. J. Hwang, S. Han, D. Choi and Y. T. Park, *ACS Energy Lett.*, 2021, **6**, 2451–2459.

22 H. G. Menge, N. D. Huynh, K. Choi, C. Y. Cho, D. Choi and Y. T. Park, *Adv. Funct. Mater.*, 2023, **33**, 2210571.

23 H. W. Park, N. D. Huynh, W. Kim, C. Lee, Y. Nam, S. Lee, K. B. Chung and D. Choi, *Nano Energy*, 2018, **50**, 9–15.

24 H. J. Hwang and D. Choi, *Funct. Compos. Struct.*, 2021, **3**, 025004.

25 M. M. Rastegardoost, O. A. Tafreshi, Z. Saadatnia, S. Ghaffari-Mosanenzadeh, C. B. Park and H. E. Naguib, *Appl. Mater. Today*, 2023, **30**, 101732.

26 C. R. Yang, C. T. Ko, S. F. Chang and M. J. Huang, *Nano Energy*, 2022, **92**, 106791.

27 B. Dudem, D. H. Kim, A. R. Mule and J. S. Yu, *ACS Appl. Mater. Interfaces*, 2018, **10**, 24181–24192.

28 X. C. Meng, X. Xiao, S. Jeon, D. Kim, B. J. Park, Y. J. Kim, N. Rubab, S. Kim and S. W. Kim, *Adv. Mater.*, 2023, **35**, 2209054.

29 R. Hinchet, H. J. Yoon, H. Ryu, M. K. Kim, E. K. Choi, D. S. Kim and S. W. Kim, *Science*, 2019, **365**, 491–494.

30 M. V. Paranjape, S. A. Graham, P. Manchi, A. Kurakula and J. S. Yu, *Small*, 2023, 2300535.

31 S. Feng, H. L. Zhang, D. L. He, Y. G. Xu, A. N. Zhang, Y. Liu and J. B. Bai, *Energy Technol.*, 2019, **7**, 1900101.

32 G. Wang, Y. Xi, H. X. Xuan, R. C. Liu, X. Chen and L. Cheng, *Nano Energy*, 2015, **18**, 28–36.

33 S. Paria, S. K. Si, S. K. Karan, A. K. Das, A. Maitra, R. Bera, L. Halder, A. Bera, A. De and B. B. Khatua, *J. Mater. Chem. A*, 2019, **7**, 3979–3991.

34 S. Hajra, A. M. Padhan, M. Sahu, P. Alagarsamy, K. Lee and H. J. Kim, *Nano Energy*, 2021, **89**, 106316.

35 Y. T. Qian, Z. Lyu, D. H. Kim and D. J. Kang, *Nano Energy*, 2021, **90**, 106536.

36 J. S. Chun, B. U. Ye, J. W. Lee, D. Choi, C. Y. Kang, S. W. Kim, Z. L. Wang and J. M. Baik, *Nat. Commun.*, 2016, **7**, 12985.

37 S. K. Singh, P. Kumar, R. Magdum, U. Khandelwal, S. Deswal, Y. More, S. Muduli, R. Boomishankar, S. Pandit and S. Ogale, *ACS Appl. Bio Mater.*, 2019, **2**, 3164–3170.

38 B. Dudem, S. A. Graham, R. D. I. G. Dharmasena, S. R. P. Silva and J. S. Yu, *Nano Energy*, 2021, **83**, 105819.

39 N. A. S. M. Pu'ad, P. Koshy, H. Z. Abdullah, M. I. Idris and T. C. Lee, *Heliyon*, 2019, **5**, e01588.

40 M. R. Ayatollahi, M. Y. Yahya, H. A. Shirazi and S. Abu Hassan, *Ceram. Int.*, 2015, **41**, 10818–10827.

41 M. Akram, R. Ahmed, I. Shakir, W. A. W. Ibrahim and R. Hussain, *J. Mater. Sci.*, 2014, **49**, 1461–1475.

42 D. L. Goloshchapov, V. M. Kashkarov, N. A. Rumyantseva, P. V. Seredin, A. S. Lenshin, B. L. Agapov and E. P. Domashevskaya, *Ceram. Int.*, 2013, **39**, 4539–4549.

43 K. Alorku, M. Manoj and A. H. Yuan, *RSC Adv.*, 2020, **10**, 40923–40939.

44 J. Klinkaewnarong and S. Utara, *Ultrason. Sonochem.*, 2018, **46**, 18–25.

45 S. Swain, A. S. Muneer, R. Sahu, A. Mahapatra, R. R. Negi, B. Samanta, D. Nanda, P. Kumar, S. Dasgupta and S. Sonia, *Integr. Ferroelectr.*, 2020, **205**, 186–193.

46 K. P. Tank, P. Sharma, D. K. Kanchan and M. J. Joshi, *Cryst. Res. Technol.*, 2011, **46**, 1309–1316.

47 J. Q. Xu, Y. Q. Yang, R. Wan, Y. H. Shen and W. B. Zhang, *Sci. World J.*, 2014, 863137.

48 K. L. Lin, J. Chang, Y. J. Zhu, W. Wu, G. F. Cheng, Y. Zeng and M. L. Ruan, *Cryst. Growth Des.*, 2009, **9**, 177–181.

49 O. J. B. Ferreira, K. B. Demetrio and L. A. L. dos Santos, *Composites, Part B*, 2017, **121**, 152–161.

50 N. Verma, S. Zafar and M. Talha, *Mater. Res. Express*, 2019, **6**, 085336.

51 C. L. Custodio, P. J. M. Bronola, S. R. Cayabyab, V. U. Lagura, J. R. Celorico and B. A. Basilia, *Int. J. Bioprint.*, 2021, **7**, 112–122.

52 E. Hamed, Y. Lee and I. Jasiuk, *Acta Mech.*, 2010, **213**, 131–154.

53 M. Kim, B. U. Moon and C. H. Hidrovo, *J. Micromech. Microeng.*, 2013, **23**, 095024.

54 Y. L. Lin, D. L. He, H. W. Hu, P. Yi, X. T. Liu, J. H. Huang, S. Z. Wu and G. J. Li, *ACS Appl. Bio Mater.*, 2019, **2**, 4377–4384.

55 Y. Z. Zhang, K. H. Lee, D. H. Anjum, R. Sougrat, Q. Jiang, H. Kim and H. N. Alshareefit, *Sci. Adv.*, 2018, **4**, eaat0098.

56 X. S. Zhang, M. D. Han, R. X. Wang, B. Meng, F. Y. Zhu, X. M. Sun, W. Hu, W. Wang, Z. H. Li and H. X. Zhang, *Nano Energy*, 2014, **4**, 123–131.

57 K. N. Kim, Y. K. Jung, J. Chun, B. U. Ye, M. Gu, E. Seo, S. Kim, S. W. Kim, B. S. Kim and J. M. Baik, *Nano Energy*, 2016, **26**, 360–370.

58 S. Iqbal, M. Younas, M. ul Hassan, H. J. Ryu, M. A. R. Anjum, M. A. Farhan, M. Nadeem and J. I. Yun, *Chem. Phys. Lett.*, 2021, **771**, 138507.

59 S. Krohns, P. Lunkenheimer, S. Meissner, A. Reller, B. Gleich, A. Rathgeber, T. Gaugler, H. U. Buhl, D. C. Sinclair and A. Loidl, *Nat. Mater.*, 2011, **10**, 899–901.